



Mathematical modeling of MILD combustion of pulverized coal

N. Schaffel^{a,b}, M. Mancini^b, A. Szlęk^a, R. Weber^{b,*}

^aSilesian University of Technology, Institute of Thermal Technology, Konarskiego 22, 44-101 Gliwice, Poland

^bClausthal University of Technology, Institute of Energy Process Engineering and Fuel Technology, Agricolastrasse 4, 38678 Clausthal-Zellerfeld, Germany

ARTICLE INFO

Article history:

Received 8 December 2008

Received in revised form 8 April 2009

Accepted 16 April 2009

Available online 26 May 2009

Keywords:

MILD (flameless) combustion

Coal combustion

NO_x emissions

CFD

ABSTRACT

MILD (flameless) combustion is a new rapidly developing technology. The IFRF trials have demonstrated high potential of this technology also for N-containing fuels. In this work the IFRF experiments are analyzed using the CFD-based mathematical model. Both the Chemical Percolation Devolatilization (CPD) model and the char combustion intrinsic reactivity model have been adapted to Guasare coal combusted. The flow-field as well as the temperature and the oxygen fields have been accurately predicted by the CFD-based model. The predicted temperature and gas composition fields have been uniform demonstrating that slow combustion occurs in the entire furnace volume. The CFD-based predictions have highlighted the NO_x reduction potential of MILD combustion through the following mechanism. Before the coal devolatilization proceeds, the coal jet entrains a substantial amount of flue gas so that its oxygen content is typically not higher than 3–5%. The volatiles are given off in a highly sub-stoichiometric environment and their N-containing species are preferentially converted to molecular nitrogen rather than to NO. Furthermore, there exists a strong NO-reburning mechanism within the fuel jet and in the air jet downstream of the position where these two jets merge. In other words, less NO is formed from combustion of volatiles and stronger NO-reburning mechanisms exist in the MILD combustion if compared to conventional coal combustion technology.

© 2009 Published by Elsevier Inc. on behalf of The Combustion Institute.

1. Introduction and objectives

Coal is an abundant fuel resource in many of the developing regions and forecasts show that it is likely to remain a dominant fuel for electricity generation in many countries for years to come. Coal-fired power plants currently generate approximately 40% of the world electricity. Since coal dominates the energy supply in the developing countries and still is an important fuel in the industrialized nations it will continue to play an important role in worldwide power generation [1]. Thus, the development of advanced coal combustion technologies of a higher performance efficiency and lower pollutant emissions is a major goal of combustion researchers.

MILD (Moderate and Intensive Low-oxygen Dilution) combustion (often written simple as mild combustion), named also FLameless OXidation – FLOX or High Temperature Air Combustion – HTAC, is probably the most important achievement of combustion technology in recent years. Within a decade or two, it has been developed from laboratory tests to industrial applications which certainly is an extraordinary progress as for an energy technology. A comprehensive review paper summarizing both the development and current status of this technology does not exist although some information can be found in [2–5]. The essence of this tech-

nology is that fuel is oxidized in an environment that contains a substantial amount of inert (flue) gases. For clean gaseous fuels that do not contain any fuel-bounded nitrogen this results in very low NO_x emissions even if the combustion air stream is preheated to temperatures in excess of 1000 °C. Chemical reactions take place in almost the entire volume of the combustion chamber and uniformity of both the temperature and the chemical species fields are characteristics of this technology.

1.1. MILD combustion of coal

The International Flame Research Foundation (IFRF) carried out perhaps the first experiment on applicability of the MILD combustion concept to pulverized coal firing [6–8]. A high volatile coal (1.4% N) was combusted with high temperature air and the lowest NO_x emissions were in the range 160–175 ppm (at 3% O₂) indicating high NO_x reduction potential of this technology also for nitrogen containing fuels (for details see paragraph 2 below).

A pulverized coal FLOX burner is currently under development in the frame of an EU project [9]. The tests have been carried out in a drop tube furnace, in a bench-scale reactor (5–8 kW) at the University of Stuttgart and in a pilot-scale rig (40–60 kW) at RWTH Aachen [10,11]. The burner combines the FLOX technique together with air staging. The primary air and pulverized coal are injected into the furnace via a central pipe. The secondary air is provided through nozzles located on the circumference of the primary jet

* Corresponding author. Fax: +49 5323 724863.

E-mail address: roman.weber@ievb.tu-clausthal.de (R. Weber).

while the tertiary (burnout) air is injected downstream. Under optimized firing conditions, the NO_x concentrations were below 200 mg/m^3 (at 6% O_2) and the carbon monoxide concentrations were as low as 30 mg/m^3 (at 6% O_2). While firing Lausitz lignite a high degree of burnout (carbon in ash <0.3%) has been measured, however burnout problems have occurred for hard Budryk and Kleinkopje coals (carbon in ash <18.9%) [10,11]. Coal behavior under MILD combustion conditions has also been researched at the Ruhr-University Bochum [12,13] to gain a better understanding of NO_x formation and reduction mechanisms. The data on volatile matter release, volatiles composition, and char are determined by flash pyrolysis investigations.

MILD combustion of pulverized coal was experimentally investigated by Suda et al. [14]. Flame stability, ignition delay, char burnout, and NO_x emission were examined using a 250 kW furnace. The combustion air was preheated to a temperature of either 623 or 1073 K. The authors concluded that the ignition delay decreased dramatically with increasing air temperature. Stable combustion was obtained even for an anthracite. The peak temperature of the flames remained unaltered when the air preheat was increased from 623 to 1073 K. NO_x emissions of 1000 and 400 ppm were measured for the 623 and 1073 K air temperature, respectively. Thus, a 40% NO_x emissions reduction was observed when the combustion air temperature increased. However, the absolute NO_x emissions were substantially larger than these obtained in the IFRF experiment [6].

Numerical studies of MILD coal combustion were performed by He et al. [15] who modeled Suda's experiments [14]. The goal was to study NO_x formation and destruction mechanisms. The free jet theory was used to describe the flow field. It was assumed that during pyrolysis the coal nitrogen was released to volatiles as HCN or remained in the char. The thermal mechanism of NO_x formation was also considered. The model incorporated three NO destruction paths: the reactions with HCN, char and soot. It was concluded that 90% of the NO_x emissions were formed through the fuel path and the remaining 10% through the thermal route.

The experiment on MILD coal combustion under high pressure (3 bar) conditions was carried out by Heil et al. [16] and modeled by Erfurth et al. [17] using the CFD FLUENT code. Three-dimensional steady-state simulations of a 1/6-sector of the furnace were performed for lignites and bituminous coals. Standard sub-models implemented in the FLUENT code were used; the Eddy Dissipation Concept with two global reactions for turbulence–chemistry interaction modeling and P1 or Discrete Ordinates models for radiation. A Lagrangian description for the solid phase was used. Very simple empirical sub-models were used for devolatilization (constant rates) and char burnout (diffusion-kinetics limited). This simple mathematical model was able to predict well the flow field and the recirculation inside the combustion chamber. The temperatures were over-predicted in comparison with the experimental data while the species concentrations differed substantially from the measured values. Needs for detailed sub-models for devolatilization and char burnout became apparent.

The IFRF experiments on MILD coal combustion technology [6] were simulated by Kim et al. [18,19]. The objective was to investigate the ability of the CFD AIOLOS code to predict the nitrogen oxide levels. Three-dimensional simulations of a quarter of the furnace were performed under steady-state conditions. The coal combustion was modeled including primary and secondary pyrolysis, volatile combustion, and char burnout, using sub-models described by Försch [20,21]. All the gas phase reactions were calculated using global mechanisms. The pyrolysis gas was represented by CH_4 while the tar was approximated as $\text{C}_x\text{H}_y\text{O}_z$. The secondary reactions of tar were modeled by three competing reactions yielding soot, hydrogen, light hydrocarbons, and carbon monoxide. The pyrolysis products were predicted using the Functional Group-Depolymerization

Vaporization Cross linking (FG-DVC) model [22] which allowed for predictions of both the yield and the composition of products of primary pyrolysis. The NO_x formation modeling included fuel and thermal mechanisms. The release of volatile nitrogen was assumed to follow the rate of primary pyrolysis and HCN and NH_3 were the primary N-containing species of the pyrolysis gas. The release of char nitrogen was enhanced in the initial stages of char combustion and char nitrogen was released not only as intermediate NH_3 but also directly as NO, depending on a mechanism factor defined by Försch [20]. The char-NO production was proportional to the rate of CO formation in char oxidation. The interaction between chemistry and turbulence was modeled using the Eddy Dissipation Concept. Turbulence was calculated using the standard k – ϵ model whilst radiative heat transfer by a Discrete Ordinates method. An Eulerian description for the solid phase was used. Generally, good agreement between experimental data and simulation results was achieved. However, the carbon monoxide concentrations were strongly over-estimated inside the combustion chamber and at the furnace exit. Throughout the furnace and at the furnace exit too high oxygen concentrations were computed while the carbon dioxide concentrations were under-estimated. The numerical model slightly under-estimated the NO_x values within the combustion zone. The authors concluded that there was a need for the development of detailed coal combustion models.

1.2. Objectives

The experiments [6–8] resulted not only in the lowest NO_x emissions achieved in the 40-years long IFRF history of burner development for pulverized coal combustion but also initiated a new burner/furnace design methodology. Thus, it is important to gain a good insight into the NO_x formation and destruction mechanisms of the MILD combustion in order to identify features that distinct this new technology from conventional low- NO_x firing. To obtain such an insight we use our CFD-based mathematical modeling software and the IFRF experiments [6–8,23]. At the same time, a comparison of the model predictions against the measured data provides a validation of several sub-models as for their predictability of this emerging technology.

2. The IFRF experiment

The experiments [6–8] were executed in a refractory lined IFRF furnace No. 1 shown in Fig. 1. The burner consisted of a central 125 mm diameter pipe supplying the oxidizer and two 27.3 mm coal injectors (pipes) which were located 280 mm away from the burner center, as shown in Fig. 1. The burner operated at 0.58 MW fuel input and the vitiated air temperature was 1623 K, as shown in Table 1. The vitiated air stream contained 22% (wet, by weight) oxygen and 89 ppm (wet, by weight) NO. The vitiated air and the coal streams were supplied into the furnace with injection velocities of 65 and 26 m/s, respectively.

The measurements were taken at several traverses (Fig. 1) in a horizontal plane cutting through the burner centerline. In-flame measurements included mean and rms axial velocities, gas temperature, gas composition (CO_2 , O_2 , CO, NO_x , C_mH_m), burnout, solids concentrations, total radiance and total radiative fluxes at the furnace wall. The velocity measurements were performed using the IFRF water cooled Laser Doppler Velocimetry (LDV) probe. In-flame temperatures were measured using a suction pyrometer equipped with a type B thermocouple (Pt6%Rh/Pt30%Rh). Local in-flame gas compositions were measured using a gas sampling probe. The measurements of total radiance and total radiative heat fluxes were performed using a standard IFRF narrow angle radiometer and an ellipsoidal radiometer, respectively. Detailed description of these measurements can be found in [6,7].

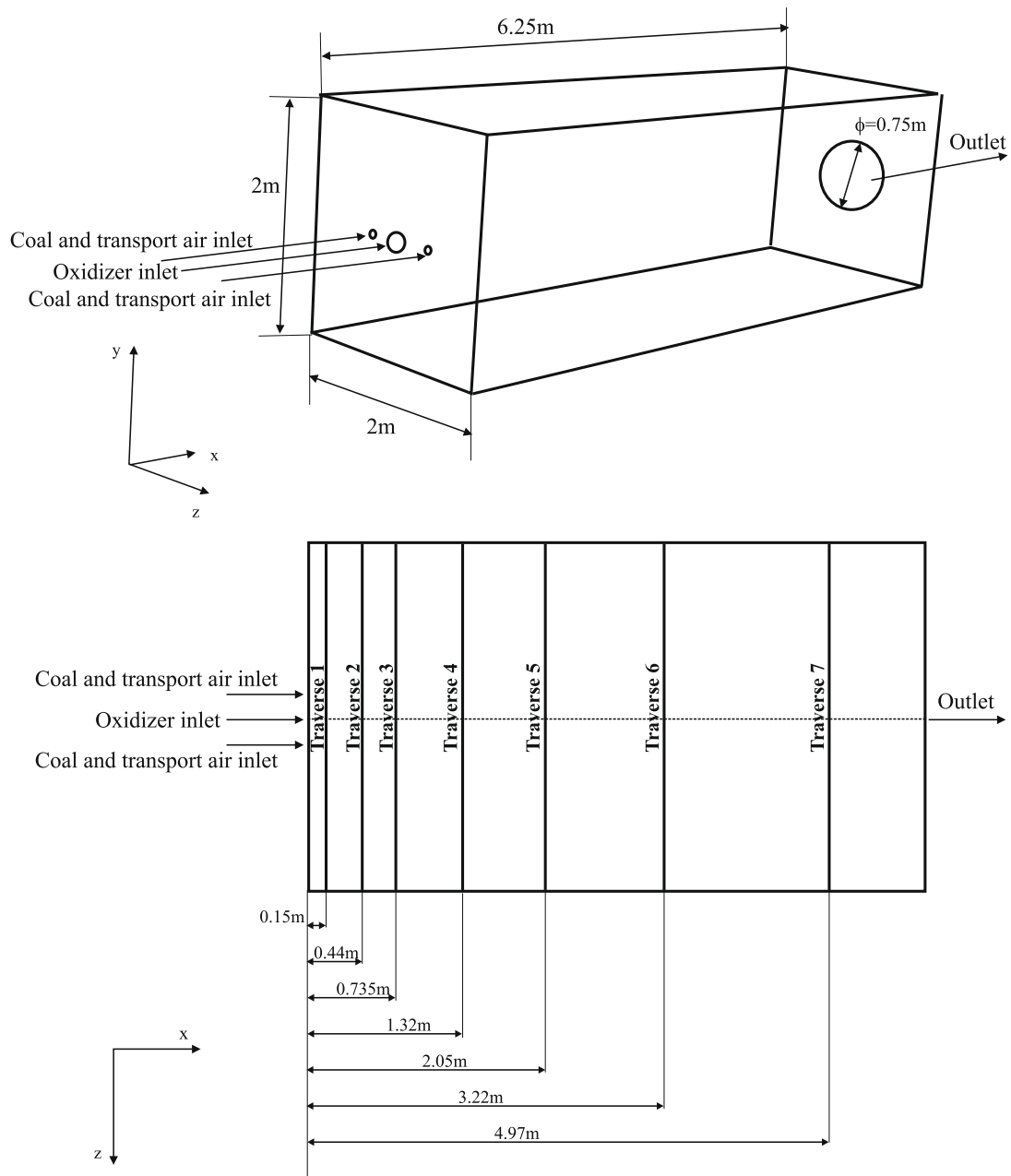


Fig. 1. Geometry of the IFRF furnace No. 1; location of the measurement traverses.

Table 1
Experimental conditions.

	Mass flow (kg/h)	Vel. (m/s)	Temp. (K)	Enthalpy (MW)	Composition (wt% wet)
Coal	66	–	–	0.58	
Coal transport air	130	26	313	–	O ₂ = 23, N ₂ = 77
Oxidizer (vitiated air)	675	65	1623	0.30	O ₂ = 22, H ₂ O = 9.5, CO ₂ = 12.5, NO = 89×10^{-4} , N ₂ = 56
Furnace exit	871	30	1503	0.36	O ₂ = 2.8, H ₂ O = 11, CO ₂ = 31, NO = 250×10^{-4} , N ₂ = 55.2

3. Mathematical model

The CFD FLUENT code (version 6.3) has been used in our work as the modeling software. Substantial efforts have been allocated into a proper numerical description of the coal combustion. To this end several fuel specific subroutines have been developed and these are described in detail in Section 3.1. Sections 3.2–3.4 provide just a very brief description of the sub-models used.

3.1. Numerical description of the coal combustion

The Venezuelan bituminous Guasare coal was combusted [6]. According to the ASTM classifications it is a high volatile bituminous A coal. The proximate and ultimate analysis of Guasare coal are given in Tables 2 and 3, respectively.

The coal was milled to give a particle size distribution of 80% < 90 μm . The Rosin-Rammler distribution function with the

Table 2
Guasare coal proximate analysis.

Composition	wt%
Moisture (105 °C)	2.9
Volatile matter	37.1
Fixed carbon	56.7
Ash	3.3
LCV	31.74 (MJ/kg)

Table 3
Guasare coal ultimate analysis (dry, ash free basis).

Composition (wt% daf)	Coal	Char	Volatiles
C	81.6	92.6	72.51
H	5.5	1.3	9.10
N	1.5	1.7	1.3
O	10.7	4.0	16.3
S	0.6	0.4	0.8

mean diameter of 42 μm and the spread of 1.36 represents nicely the measured data, as shown in Fig. 2. In the CFD predictions of this work, the 10–300 μm size range has been divided into 20 size classes and around 750 particles are injected per class each time the particle tracking procedure is activated.

In contrast to the empirical devolatilization models (for example a single rate model [24], Kobayashi model [25]), the Chemical Percolation Devolatilization (CPD) model [26–28] characterizes the devolatilization behavior of a rapidly heated coal particle on the basis of the physical and chemical transformations of the structure. Modeling the cleavage of the bridges and the generation of light gas, char, and tar precursors is then considered to be analogous to the chemical reaction scheme shown in Fig. 3.

The variable ξ represents the original population of labile bridges in the coal lattice. Upon heating, these bridges become the set of reactive bridges. For the reactive bridges ξ^* , two competing paths are available. In one path, the bridges react to form side chains, δ . The side chains may detach from the aromatic clusters to form light gas, g_1 . As bridges between neighboring aromatic clusters are cleaved, a certain fraction of the coal becomes detached from the coal lattice. These detached aromatic clusters are the heavy-molecular-weight tar precursors that form the metaplast. The metaplast vaporizes to form coal tar. While waiting for vaporization, the metaplast can also reattach to the coal lattice matrix (crosslinking). In the other path, the bridges react and become a char bridge, c , with the release of an associated light gas product, g_2 . The total population of bridges in the coal lattice matrix can be represented by the variable p , where $p = \xi + c$.

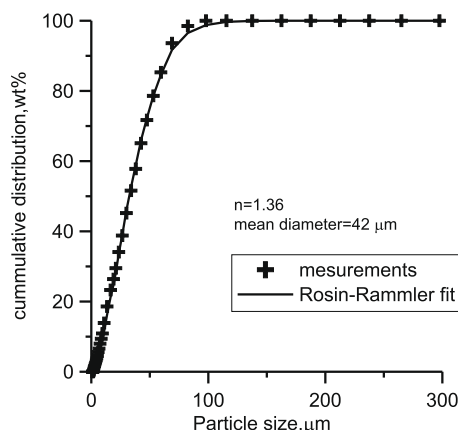


Fig. 2. Guasare coal particle distribution (left) and distribution parameters (right).

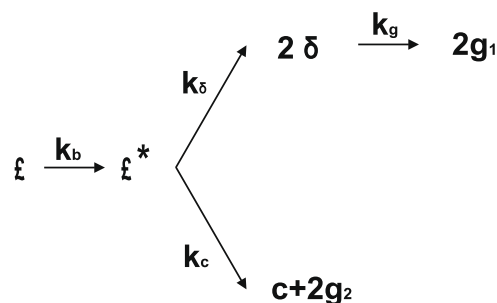


Fig. 3. Scheme of the coal behavior during devolatilization process as a simplified network of chemical bridges [27].

Table 4
The parameters for the CPD devolatilization model of Guasare coal.

Parameter	Symbol	Value	Unit
Initial fraction of bridges in coal lattice	p_0	0.5	–
Initial fraction of char bridges	c_0	0	–
Lattice coordination number	$\sigma + 1$	5	–
Cluster molecular weight	M_{cl}	300	kg/kmol
Side chain molecular weight	M_{del}	30	kg/kmol

There are five coal-specific parameters of the CPD model: the average molecular weight per aromatic cluster (M_{cl}), the average molecular weight per side chain (M_{del}), the average number of attachments per cluster, referred to as the coordination number ($\sigma + 1$), the fraction of attachments that are bridges (p_0) and initial fraction of char bridges (c_0), as shown in Table 4. The question is how to determine these five parameters for the considered coal? To this end we use other IFRF experimental data [23] on characterization of both devolatilization and char combustion of Guasare coal. Fig. 4(left) shows the devolatilization curve obtained using the IFRF Isothermal Plug Flow Reactor (IPFR) operated at a 1200 °C temperature. The particle heating rate of these experiments is in the range $10^5 \div 10^6$ K/s depending on the particle size. Under such rapid heating conditions a 55–75% high temperature yield is measured as opposed to 37% ASTM volatiles. The CPD devolatilization model has been run using as input the eight experimentally determined yields, shown in Fig. 4(left). The initial fraction of char bridges has been fixed to zero which is a typical value for bituminous coals. The obtained values of the other CPD parameters are listed in Table 4 while the CPD model devolatilization curve is shown in Fig. 4(left) using a solid line. The volatiles are represented in the CFD predictions as $C_{1.20}H_{4.48}O_{0.44}$ which provides the stoichiometric coefficient of 1.5 (see Eq. (12)).

parameter	value	unit
mean diameter	42	μm
max. diameter	300	μm
min. diameter	10	μm
spread parameter	1.36	

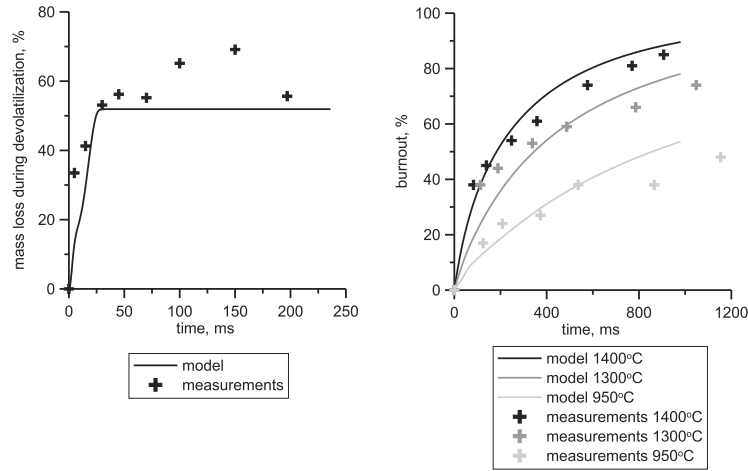


Fig. 4. Devolatilization and burnout measurements [23] with the CPD (left) and the intrinsic (right) model fittings for Guasare coal.

Char particles produced from rapid pyrolysis are microporous solids whose properties can be described by their size, true and apparent density, porosity, pore volume distribution and surface area distribution. The rate of char oxidation is controlled by sequential or parallel processes of oxygen boundary layer diffusion, chemical reaction and pore diffusion. The intrinsic model for char burnout used in this work is based on the Smith's [29] macroscopic pore model which assumed that the char oxidation reaction:



is of the first order. The overall surface reaction rate includes the effect of bulk diffusion and chemical reaction. The diffusion coefficient D_0 is computed via:

$$D_0 = C_1 \frac{[(T_p + T_\infty)/2]^{0.75}}{d_p} \quad (2)$$

The chemical rate is expressed in terms of the intrinsic chemical and pore diffusion rates:

$$\mathcal{R} = \eta \frac{d_p}{6} \rho_p A_g k_i \quad (3)$$

where d_p is the particle diameter, η the effectiveness factor, T_p the particle temperature, T_∞ the bulk temperature, ρ_p the apparent density of the char, A_g the specific internal surface area of the char particle, and k_i is the intrinsic reactivity. The effectiveness factor η is calculated as

$$\eta = \frac{3}{\phi^2} (\phi \coth \phi - 1) \quad (4)$$

where ϕ is the Thiele modulus:

$$\phi = \frac{d_p}{2} \left[\frac{S_b \rho_p A_g k_i p_{ox}}{D_e \rho_{ox}} \right]^{1/2} \quad (5)$$

and ρ_{ox} is the density of oxidant in the bulk gas, S_b is the stoichiometric coefficient in Reaction (1) in kg_{O_2}/kg_{char} and D_e is the effective diffusion coefficient in the particle pores. Assuming that the pore size distribution is unimodal and the bulk and Knudsen diffusion proceed in parallel, D_e is given by

$$D_e = \frac{\theta}{\tau^2} \left[\frac{1}{D_{Kn}} + \frac{1}{D_0} \right]^{-1} \quad (6)$$

where D_0 is the bulk molecular diffusion coefficient and θ is the porosity of the char particle:

$$\theta = 1 - \frac{\rho_p}{\rho_t} \quad (7)$$

with ρ_p and ρ_t being, respectively, the apparent and true char densities and τ is the tortuosity of the pores. A typical value for τ is $\sqrt{2}$ which corresponds to an average intersecting angle between the pores and the external surface of 45° . The Knudsen diffusion coefficient D_{Kn} is calculated as

$$D_{Kn} = 97.0 \bar{r}_p \sqrt{\frac{T_p}{M_{w,ox}}} \quad (8)$$

where T_p is the particle temperature, \bar{r}_p is the mean pore radius of the char particle, and $M_{w,ox}$ is the oxygen molecule weight. The specific internal surface area (A_g) of the char particle is assumed in this model to remain constant during char combustion. The intrinsic reactivity (k_i) is of Arrhenius form:

$$k_i = A_i e^{-(E_i/RT_p)} \quad (9)$$

where A_i is the pre-exponential factor and E_i is the activation energy.

Now we are facing the question of adapting the above char combustion model to the Guasare coal. To this end we have again used the IFRF measurements [23] of Guasare char burnout as a function of time for temperatures of 950, 1300 and 1400 °C, see Fig. 4(right). These measurements were carried out at 4% oxygen volume fraction. The measured char morphology data were: the apparent char density equal to 339 kg/m^3 and porosity equal to 74%. Fixing the mass diffusion-limited rate constant (C_1) at a value of $5 \times 10^{-12} \text{ m}^3/\text{K}^{0.75} \text{ s}$, the char porosity at the 74%, and the specific surface area at $2.5 \times 10^4 \text{ m}^2/\text{kg}$ we optimize values of both kinetic parameters A_i and E_i to obtain a proper fit to the IFRF data, as shown in Fig. 4(right). The optimization results in the values given in Table 5. Thus, in our CFD predictions presented in Paragraph 4, the initial particle diameter remains unaltered through the char combustion processes while the rate of char oxidation is calculated using Eq. (3). The char density is changing during the char burnout process according to the following equation:

$$B = \frac{(1 - \frac{\rho}{\rho_0})}{(1 - a_0)} \quad (10)$$

where ρ_0 is the initial density of char particle, a_0 is the initial ash content and B is the burnout. During the devolatilization process, macromolecules break up and formation of tar and gases can lead to swelling of the particle. In our model the swelling coefficient (C_{sw}) takes a value of 2.

To complete the model description we quote the particle energy balance which considers both the convective heat transfer and the absorption/emission of radiation at the particle surface:

Table 5

The parameters for the intrinsic char combustion model of Guasare coal.

Parameter	Symbol	Value	Unit
Mass diffusion-limited rate constant	C_1	5×10^{-12}	$\text{m}^3/\text{K}^{0.75} \text{ s}$
Pre-exponential factor	A_i	1×10^{-3}	$\text{kg}/\text{m}^2 \text{ s}$
Activation energy	E_i	5×10^7	J/kmol
Char porosity	θ	0.74	–
Mean pore radius	\bar{r}_p	1×10^{-7}	m
Specific internal surface area	A_G	2.5×10^4	m^2/kg
Tortuosity	τ	$\sqrt{2}$	–

$$m_p c_p \frac{dT_p}{dt} = h A_p (T_\infty - T_p) + \epsilon_p A_p \sigma (\theta_R^4 - T_p^4) \quad (11)$$

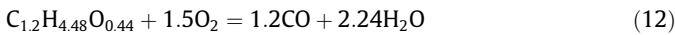
where m_p is the mass of the particle (kg), c_p the heat capacity of the particle (J/kg K), A_p the surface area of the particle (m^2), T_p the particle temperature (K), T_∞ the local temperature of the continuous phase (K), h the convective heat transfer coefficient ($\text{W}/\text{m}^2 \text{ K}$), ϵ_p the particle emissivity ($\epsilon_p = 0.8$), σ the Stefan–Boltzmann constant ($\text{W}/\text{m}^2 \text{ K}^4$), and θ_R is the radiation temperature, (K). This equation assumes that there is negligible internal resistance to heat transfer, i.e., the particle is at a uniform temperature throughout. During the char combustion the additional term $f_h \cdot \frac{dm_p}{dt} \cdot H_{\text{reac}}$ has to be added to the right hand side of Eq. (11). This term accounts for the energy release in the surface reactions (H_{reac}) which is directly absorbed by the char particle. The coefficient f_h takes a value of 0.3.

In summary of this paragraph we refer to Fig. 5 which shows the coal combustion models used in our simulations. The devolatilization is modeled using the CPD model with the model parameters listed in Table 4. The volatile matter combustion is calculated using Eqs. (12)–(15) while for the char combustion rate we use Eq. (3) with the parameters listed in Table 5.

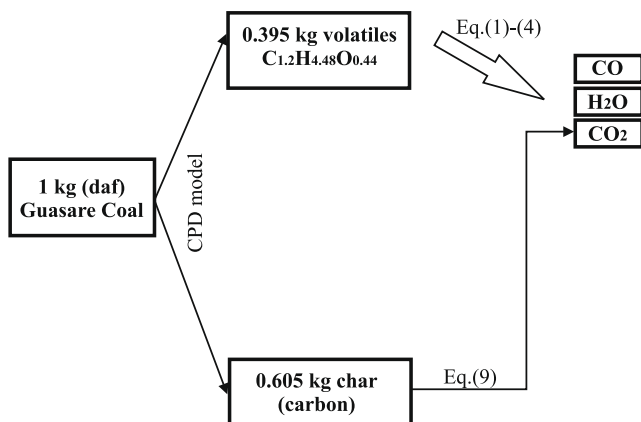
3.2. Turbulence and chemistry–turbulence interaction

The k – ϵ model [30] with the following model constants: $C_{1\epsilon} = 1.44$, $C_{2\epsilon} = 1.92$, $C_\mu = 0.09$, $\sigma_k = 1.0$, $\sigma_\epsilon = 1.3$ has been used for the flow predictions.

Combustion of the volatiles has been simplistically represented by two overall reactions:



whose rates are calculated using the Eddy Break-Up (EBU) model [31]. The rate of production or consumption of species i is then given by the smallest of the two expressions below:

**Fig. 5.** The coal combustion model used in this work.

$$R_{i,r} = v'_{i,r} M_{w,i} A \rho \left(\frac{\epsilon}{k} \right) \min \left(\frac{Y_R}{v'_{R,r} M_{w,R}} \right) \quad (14)$$

$$R_{i,r} = v'_{i,r} M_{w,i} A B \rho \left(\frac{\epsilon}{k} \right) \left(\frac{\sum_P Y_P}{\sum_j v'_{j,r} M_{w,j}} \right) \quad (15)$$

where A and B are two model empirical constants equal to 4 and 0.5, respectively. Y_P is the mass fraction of any product species (P) and Y_R is the mass fraction of the particular reactant (R); $v'_{i,r}$ is the stoichiometric coefficient for species i in reaction r ; k and ϵ are the turbulent kinetic energy and the turbulent dissipation derived from the k – ϵ model.

3.3. Particles tracking and radiation

In discrete phase modeling, coal particles of known size distributions and properties are injected into the combustion chamber and tracked in a Lagrangian fashion throughout the computational domain. The trajectory of a discrete phase particle is computed by integrating the forces acting on the particle. Only the drag and gravity forces are considered. The particle tracking procedure used in this work was developed at the beginning of the eighties at the University of Sheffield [32,33] and later on it was implemented into the FLUENT code.

The Discrete Ordinates (DO) [34,35] radiation model is used to solve the radiative heat transfer equation. The DO radiation model solves the Radiative Transfer Equation (RTE) for a finite number of discrete solid angles each associated with a vector direction \vec{s} fixed in the global Cartesian system (x, y, z). The DO model solves for as many transport equations as there are directions \vec{s} . The solution method is identical to that used for the fluid flow and energy equations. The DO model considers the radiative transfer equation in the direction \vec{s} as a field equation. This equation is written as

$$\nabla \cdot (I(\vec{r}, \vec{s}) \vec{s}) + a I(\vec{r}, \vec{s}) = a \frac{\sigma T^4}{\pi} + \frac{1}{4\pi} \int_0^{4\pi} I(\vec{r}, \vec{s}') \Phi(\vec{s} \cdot \vec{s}') d\Omega' \quad (16)$$

where \vec{r} is a position vector, \vec{s} is a direction vector, \vec{s}' is a scattering direction vector; σ is the Stefan–Boltzmann constant, T is the local temperature, I is radiation intensity, Φ –phase function and Ω' is the solid angle. The absorption coefficient (a) is prescribed a value of 1.5 m^{-1} and kept constant through the furnace volume. The value has been derived using the narrow angle radiance measured by the IFRF [6], see Section 4. The scattering has been omitted. When the solution for the RTE is known the energy source term for energy equation is calculated using the radiation flux q_r :

$$S_{\text{rad}} = -\nabla q_r \quad (17)$$

3.4. Nitric oxides

In this work the fuel, thermal, prompt and N_2O paths as well as NO reburning have been considered, as shown in Fig. 6. The transport equations for nitric oxide (NO) and for intermediate species (HCN) have been solved for while the N_2O and N-radical concentrations are calculated using the partial equilibrium assumption (see below). The sources for HCN and NO have been calculated averaging the instantaneous source term ($S_i = f(T)$) over the temperature fluctuations:

$$\langle S_i \rangle = \int_{T_0}^{T_{\text{max}}} P(T) S_i(T) dT \quad (18)$$

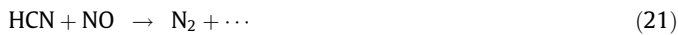
using a PDF– β function. The single-variable probability density function (PDF) approach used in our work was originally proposed by

Hand et al. [36], extended by Peters and Weber [37] and finally implemented into the FLUENT code. T_0 is the reference temperature of the system, T_{max} is the adiabatic temperature of the flame.

Since the amount of NO formed is small, the reactions involved in the NO chemistry have been separated from the pulverized coal oxidation mechanism. Thus, chemical formation and reduction rates of NO and NO-concentrations are post-processed using previously computed velocity, turbulence, temperature and chemistry fields. As shown in Fig. 6, the post-processing involves solving the NO and the HCN balance (transport) equations whose source terms are calculated as described below.

3.4.1. Fuel path

It is assumed in this work that all fuel nitrogen, both from volatiles and char, is converted into HCN that can undergo reduction or formation of NO, as shown in Fig. 6.



The HCN release rates are given by Eqs. (22) and (23), where \dot{m}_{char} and \dot{m}_{vol} are the combustion rates of char and volatile matter (in kg/s), respectively; \dot{m}_{char} is delivered by the char combustion model (the intrinsic model) and \dot{m}_{vol} is calculated using the CPD devolatilization model; V is the cell volume.

$$S_{\text{HCN},\text{char}} = \frac{\dot{m}_{\text{char}} \cdot w_{\text{N},\text{char}} \cdot M_{\text{HCN}}}{M_{\text{N}} \cdot V} \quad (\text{kg/m}^3 \text{ s}) \quad (22)$$

$$S_{\text{HCN}, \text{vol}} = \frac{\dot{m}_{\text{vol}} \cdot w_{\text{N}, \text{vol}} \cdot M_{\text{HCN}}}{M_{\text{N}} \cdot V} \quad (\text{kg/m}^3 \text{ s}) \quad (23)$$

The HCN depletion rates are given by De Soete [38] expressions:

$$r_1 = k_4 X_{\text{HCN}} X_{\text{O}_2} \exp\left(-\frac{E_4}{RT}\right) \cdot \frac{p}{RT} \quad (\text{mol/m}^3 \text{ s}) \quad (24)$$

$$r_2 = k_5 X_{\text{HCN}} X_{\text{N}_2} \exp\left(-\frac{E_5}{RT}\right) \cdot \frac{p}{RT} \quad (\text{mol/m}^3 \text{ s}) \quad (25)$$

where $k_4 = 3.5 \times 10^{10} \text{ s}^{-1}$, $k_5 = 3.0 \text{ s}^{-1}$, $E_4 = 280.5 \text{ kJ/mol}$, $E_5 = 251.2 \text{ kJ/mol}$. The instantaneous source term S_{HCN} reads then

$$S_{\text{HCN}} = S_{\text{HCN.vol}} + S_{\text{HCN.char}} - (r_1 + r_2) \cdot M_{\text{HCN}} \cdot 10^{-3} \quad (\text{kg/m}^3 \text{ s}) \quad (26)$$

and is averaged over the temperature fluctuations using Eq. (18).

The NO source term from fuel nitrogen is expressed as follows:

$$S_{NO_{fuel}} = (r_1 - r_2) \cdot M_{NO} \cdot 10^{-3} \quad (\text{kg/m}^3 \text{ s}) \quad (27)$$

3.4.2. Prompt path

De Soete [38] proposed a roughly estimated chemical reaction rate for prompt NO formation:

$$r_6 = f \cdot A \cdot [\text{O}_2]^b [\text{N}_2] [\text{C}_x\text{H}_y] \exp\left(-\frac{E_a}{RT}\right) \cdot V \quad (\text{mol/m}^3 \text{ s}) \quad (28)$$

where the exponent b may vary between 0 and 1, and depends on the conditions in the flame, namely the local mole fraction of oxygen $[O_2]$:

$$b = \begin{cases} 1.0, & [\text{O}_2] \leq 4.1 \times 10^{-3} \\ -3.95 - 0.9 \ln[\text{O}_2], & 4.1 \times 10^{-3} \leq [\text{O}_2] \leq 1.11 \times 10^{-2} \\ -0.35 - 0.1 \ln[\text{O}_2], & 1.11 \times 10^{-2} < [\text{O}_2] < 0.03 \\ 0, & [\text{O}_2] \geq 0.03 \end{cases}$$

The constant A and activation energy E_a take the following values: $A = 6.4 \times 10^6 \left(\frac{RT}{p}\right)^{b+1}$, $E_a = 303.5$ kJ/mol. The prompt factor f accounts for the type of fuel and is calculated in the following way [39]:

$$f = 4.75 + 0.0819 \cdot c - 23.2 \frac{1}{\lambda} + 32 \frac{1}{\lambda^2} - 12.2 \frac{1}{\lambda^3}$$

where c is the number of carbon atoms per molecule of fuel and is assumed to be $c = 1.2$ for the volatile matter of the Guasare coal and λ is the air excess ratio.

The NO source term for prompt path reads then

$$S_{\text{NO,prompt}} = r_6 \cdot M_{\text{NO}} \cdot 10^{-3} \quad (\text{kg/m}^3 \text{ s}) \quad (29)$$

3.4.3. Thermal path

The extended Zeldovich mechanism incorporates the following reactions:

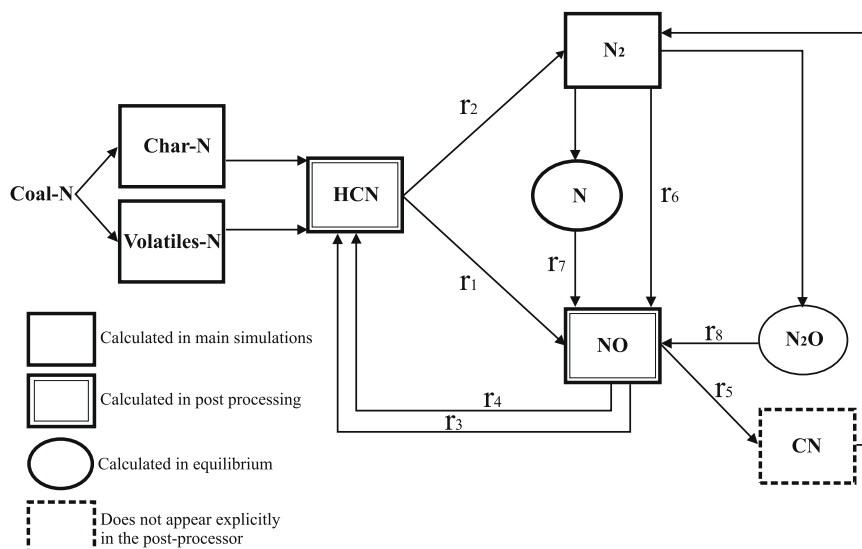


Fig. 6. Path of NO formation and reburning.

where k_{+1}, k_{+2}, k_{+3} stand for the forward and k_{-1}, k_{-2}, k_{-3} for the backward rate constants corresponding to Reactions (30)–(32). Under the assumption of partial equilibrium for N-radical, the NO formation rate can then be calculated as

$$r_7 = 2k_{+1}[O][N_2] \frac{1 - \frac{k_{-1}k_{-2}[NO]^2}{k_{+1}[N_2]k_{+2}[O_2]}}{1 + \frac{k_{-1}[NO]}{k_{+2}[O_2] + k_{+3}[OH]}} \cdot V \quad (\text{mol/m}^3 \text{ s}) \quad (33)$$

The O and OH radical concentrations are calculated by assuming equilibrium of the following reactions:



Finally, the NO source term for thermal path reads

$$S_{NO,thermal} = r_7 \cdot M_{NO} \cdot 10^{-3} \quad (\text{kg/m}^3 \text{ s}) \quad (36)$$

3.4.4. N_2O path

In low temperature combustion (below 1500 K) of lean mixtures of hydrocarbons (or at pressures higher than the atmospheric) a mechanism, in which the N_2O molecule is the intermediary, becomes important [40]. The concentration of N_2O is assumed to be in a quasi-steady state:

$$[N_2O] = \frac{k_{n1}[N_2][O][M] + k_{n2}[NO]^2}{(k_{n2} + k_{n3})[O] + (k_{n4} + k_{n5})[H]} \quad (37)$$

Assuming that the N_2O is converted to NO the rate of NO formation is

$$r_8 = 2[N_2O](k_{n2}[O] + k_{n4}[H]) \cdot V \quad (\text{mol/m}^3 \text{ s}) \quad (38)$$

where

$$[M] = 1.4 \cdot [O_2] + 3.0 \cdot [CO_2] + 1.7 \cdot [N_2] + 12 \cdot [H_2O]$$

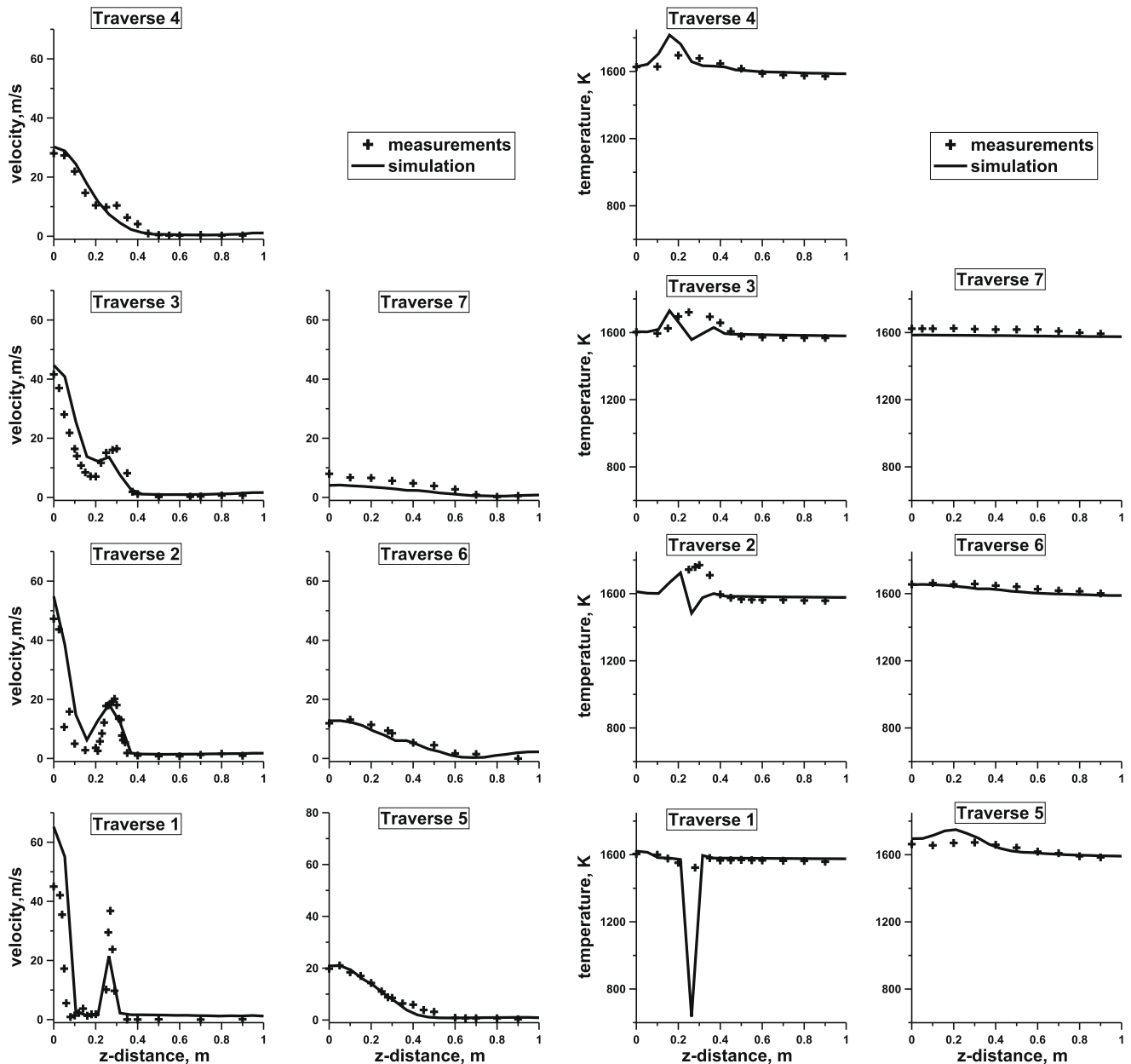


Fig. 7. Velocity (left) and temperature (right) profiles along the measurement traverses. The measured values taken from [6]. For location of the measurement traverses see Fig. 1.

Then, the NO source term for N₂O path is calculated as

$$S_{\text{NO},\text{N}_2\text{O}} = r_8 \cdot M_{\text{NO}} \cdot 10^{-3} \quad (\text{kg/m}^3 \text{ s}) \quad (39)$$

3.4.5. Reburning in gaseous phase

Following the work of Chen et al. [41,42] the major reburning reactions are



and in this work it is assumed that the volatile matter is the reburning agent, so the global NO reduction rates are

$$r_4 = 4 \times 10^{-4} \cdot (k_9 + k_{10}) [\text{C}_{1.2}\text{H}_{4.4}\text{O}_{0.44}] [\text{NO}] \quad (\text{mol/m}^3 \text{ s}) \quad (43)$$

$$r_5 = 4 \times 10^{-4} \cdot k_{11} [\text{C}_{1.2}\text{H}_{4.4}\text{O}_{0.44}] [\text{NO}] \quad (\text{mol/m}^3 \text{ s}) \quad (44)$$

where $k_9 = 5.30 \times 10^9 \cdot T^{-1.54} \cdot \exp(-\frac{27,977}{RT})$, $k_{10} = 3.31 \times 10^{13} \cdot T^{-3.33} \cdot \exp(-\frac{15,090}{RT})$, $k_{11} = 1.356 \times 10^{12} \cdot T^{-2.64} \cdot \exp(-\frac{144,090}{RT})$. Then, the source term for NO reburning is calculated as

$$S_{\text{NO},\text{hom.reburn}} = -(r_4 + r_5) \cdot M_{\text{NO}} \cdot 10^{-3} \quad (\text{kg/m}^3 \text{ s}) \quad (45)$$

3.5. Reburning on char particles

The heterogeneous reduction of NO on the char surface is modeled following the work of Levy et al. [43]:

$$r_3 = -k_6 \cdot X_{\text{NO}} \cdot p \cdot \exp\left(-\frac{E_6}{RT}\right) \cdot c_s \cdot A_g \quad (\text{mol/m}^3 \text{ s}) \quad (46)$$

where A_g is the (BET) specific surface area and c_s is the solid matter concentration and: $k_6 = 2.27 \times 10^{-3} \text{ mol/Pa m}^2$, $E_6 = 142.7 \text{ kJ/mol}$. The source term for NO-reburning on the char particles is expressed as follows:

$$S_{\text{NO},\text{het.reburn}} = r_3 \cdot M_{\text{NO}} \cdot 10^{-3} \quad (\text{kg/m}^3 \text{ s}) \quad (47)$$

Thus, considering the above-mentioned mechanisms of NO formation and destruction, the instantaneous source term for the NO transport equation is evaluated as

$$S_{\text{NO}} = S_{\text{NO},\text{fuel}} + S_{\text{NO},\text{prompt}} + S_{\text{NO},\text{thermal}} + S_{\text{NO},\text{N}_2\text{O}} + S_{\text{NO},\text{hom.reburn}} + S_{\text{NO},\text{het.reburn}} \quad (48)$$

Obviously, the above source term is then averaged over temperature fluctuations using Eq. (18).

4. Results and discussion

A quarter of the furnace has been modeled only taking advantage of the symmetry. An unstructured mesh consisting of 700,000 cells has been used with the small cell size being around 2 mm and the largest around 75 mm. For numerical representation of the central jet inlet area 600 cells have been used while the small fuel jet inlet area has been represented by 150 cells. Convergence has been achieved after performing around 50,000 iterations. A grid sensitivity study was performed and two grids consisting of 700,000 and 2,500,000 cells were tested. Predictions using both grids did not differ by more than few percent and the smaller grid has been used for all simulations presented below.

4.1. Flow field and recirculation

In Fig. 7(left) the measured and calculated velocities along the seven traverses are shown. At the first traverse the computed val-

ues correspond well with the measured velocities except for the combustor centerline velocities which were measured about 20 m/s lower than the calculated values. Here the measured values are obviously incorrect. For a 128 mm diameter jet of 65 m/s inlet velocity, at $x/d = 1.2$ which is in the jet potential core, the velocity must be still around 65 m/s. At the first two traverses the combustor jet can be clearly distinct from the coal jet. The coal jet merges into the combustor jet near the third traverse. Downstream of the third traverse both jets merge and form one stream that can be observed at the next traverses. At a distance of 2 m downstream of the furnace front wall (from the fifth traverse onwards) the velocity profile is flat. As shown in Fig. 7(left) the size of the recirculation region formed in the furnace and its low magnitude (negative) velocities are well reproduced in the computation. Gen-

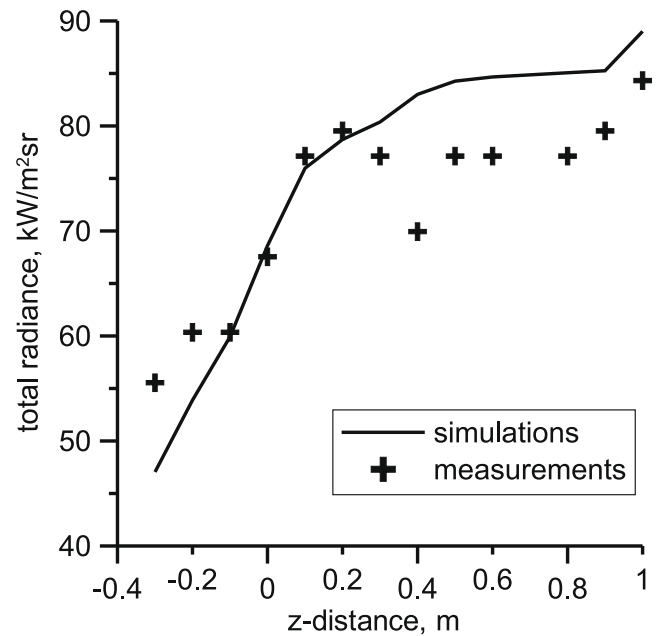


Fig. 8. Measured [6] and calculated total radiation intensity for $a = 1.5 \text{ m}^{-1}$.

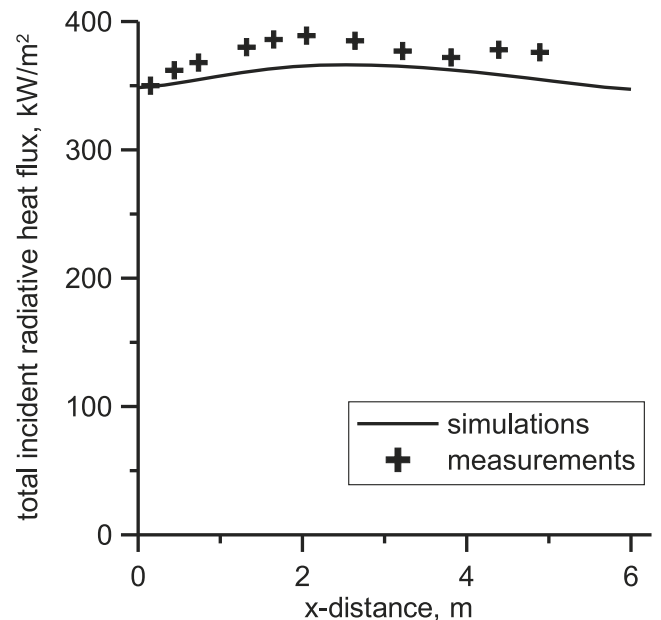


Fig. 9. Measured [6] and calculated total incident radiative heat flux.

erally, the velocity predictions (the flow field together with the recirculation) are in good agreement with the measurements.

4.2. Temperature field and radiative heat fluxes

The temperature profiles along the traverses are given in Fig. 7(right). No substantial difference between the model predictions and the measurements can be seen with exception of the fuel jet at the first traverse. The temperature level, as well as the temperature peaks are reproduced well by the simulations. Ignition of the fuel jet takes place somewhere between the first and the second traverse so that the peak temperature of around 1800 K occurs between the second and third traverses. This feature is again well reproduced in the numerical simulations. From the fourth traverse downwards, the temperature profile is flat since slow combustion proceeds downstream in the furnace and the temperature level is everywhere around 1600 K. Generally, the agreement between the temperature predictions and the measurements is quite satisfactory.

To obtain such a good accuracy of the temperature predictions it is imperative that the value of the absorption coefficient appearing in Eq. (16) is properly selected. Following the method of Lalle-mant et al. [44] and Sayre et al. [45] we use here the narrow angle radiance measured at the fifth traverse (2.05 m). Fig. 8 shows that using a value of 1.5 m^{-1} which accounts for the $\text{CO}_2/\text{H}_2\text{O}$ radiation as well as for soot and particles radiation, the predicted and measured radiation intensities are in good agreement. The verification of the correctness of the radiative heat transfer procedure is demonstrated in Fig. 9 showing very good agreement between the measured and the predicted total incident heat flux at the furnace wall. Flatness and high values of the radiative heat flux are characteristics of mild combustion [46,47].

4.3. Oxygen and carbon dioxide concentration fields

In Fig. 10(left) the profiles of oxygen concentration are shown. No major differences between the measurements and calculated

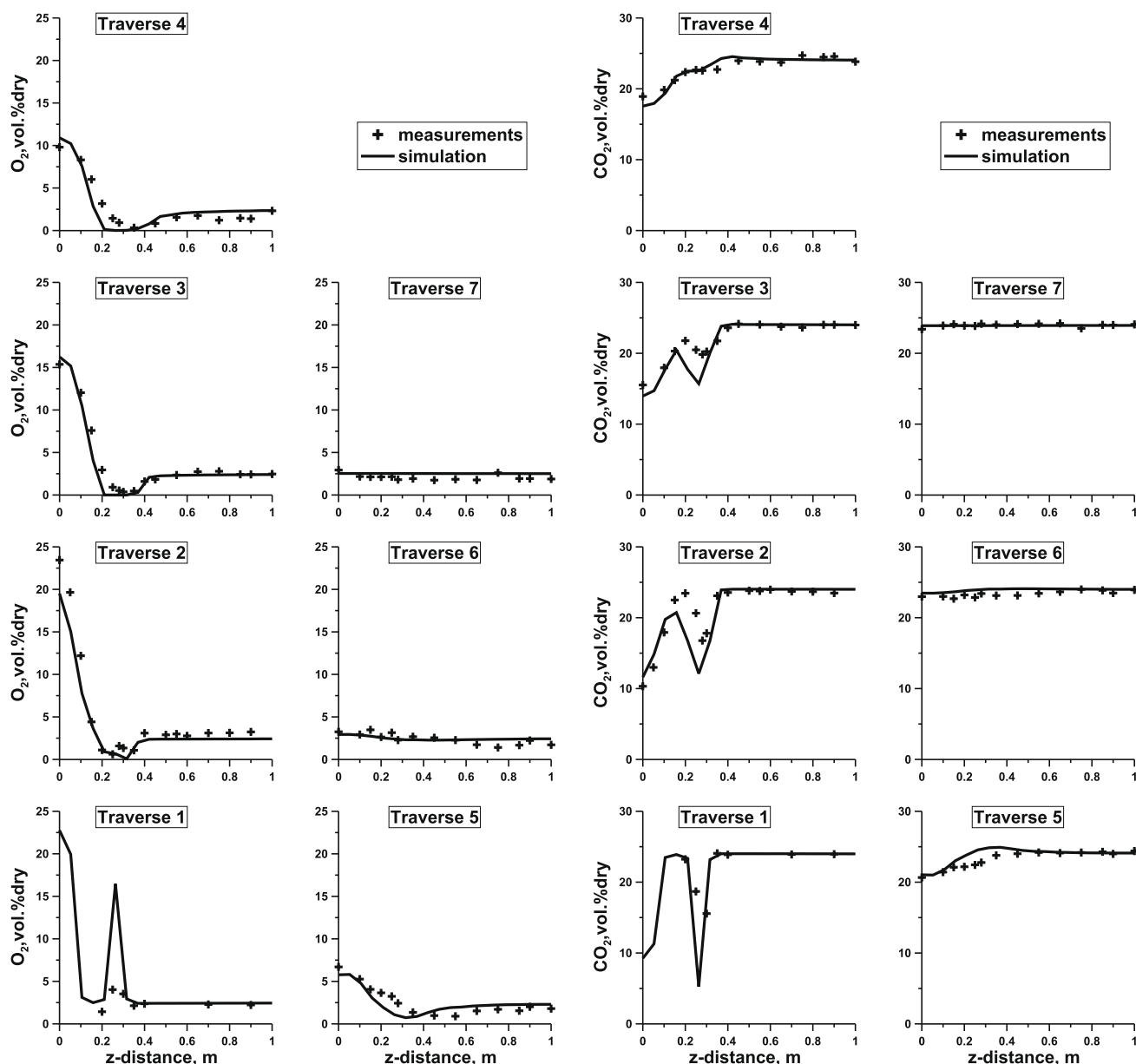


Fig. 10. Oxygen (left) and carbon dioxide (right) concentration profiles along the measurement traverses. The measured values taken from [6]. For location of the measurement traverses see Fig. 1.

values can be observed. However the oxygen concentrations near the coal nozzle are too low in comparison with the experimental values which is consistent with the temperature predictions in this region, see Fig. 7(right). It is interesting to note that the same model deficiency was already observed in numerical simulations of the natural gas combustion [47] and it was related to inaccurate predictions of the entrainment of the fuel jet [48]. Downstream of the fourth traverse the oxygen concentration is uniform and practically everywhere in the furnace is about 3%. Altogether, the numerical predictions of oxygen concentration and the measurements are in good agreement. Carbon dioxide profiles are given in Fig. 10(right). The calculated values are very close to the measured values along all traverses.

4.4. Carbon monoxide concentration field

Carbon monoxide profiles are illustrated in Fig. 11(left). In our simulations carbon monoxide is generated from the combustion of volatiles only. If oxygen is available it can be further oxidized to carbon dioxide. It is formed mostly within the coal jet up to the forth traverse. The highest concentration of CO is about 6% and it is located at the third traverse. The prediction of its peak value agrees perfectly with the measurement. Downstream of the fifth traverse no considerable amount of carbon monoxide is detectable. Although the carbon monoxide predictions are in very good agreement with the measured values, we regard this agreement as coincidental for several reasons. The monoxide is formed and oxidized in a number of sequential and parallel reactions. It is released as a component of the volatiles, as a product of the volatiles oxidation, and as a product of char combustion. The monoxide is oxidized by OH radicals as well as by O radicals, although with much lower a rate. Furthermore, the water gas shift reaction alters CO concentrations. None of these processes are taken into account in our modeling. Thus, from the fundamental point of view, the works of Kim et al. [18,19] are superior since their attempt to take these CO-involving reactions into account although the CO-predictions in Kim's simulations depart from the measured values.

4.5. Nitric oxide concentration field

Nitric oxide concentration profiles are given in Fig. 12(left) showing that the concentrations of NO are reasonably well predicted by the model, not only qualitatively but also quantitatively. It can be observed that the NO formation begins upstream of the first traverse, however most of the NO is formed upstream of the third traverse in the volatiles released zone. At the second traverse the highest peak of 900 ppm has been measured. This peak is also well reproduced in the calculations. Downstream of the fourth traverse the nitric oxide profile is flat and of a low level (around 300 ppm). At the outlet 333 ppm NO was calculated and this value agrees very well with the measurements (320 ppm).

Among the six terms which appear in Eq. (48) for the net NO formation rate only the fuel-NO source (Eq. (27)), the homogenous NO-reburning source (Eq. (45)) and heterogenous NO-reburning source (Eq. (47)) are significant and there are plotted in Fig. 12. The fuel-NO source, $S_{NO,fuel}$, is of the order of $0 \div 7.8 \times 10^{-4}$ kmol/m³s while the homogenous NO-reburning rate, $S_{NO,hom.reburn}$, is in the range of $-2.7 \times 10^{-4} \div 0$ kmol/m³s and the heterogenous NO-reburning rate, $S_{NO,heter.reburn}$, is in the range of $-2.0 \times 10^{-4} \div 0$ kmol/m³s. Thus, these three sources are of the same order of magnitude and the in-flame NO-concentrations are determined by their balance which is then altered due to the NO advection and diffusion. The NO post-processor predicts a rapid reburning occurring already in the fuel jet where NO is formed directly from HCN decomposition. Examining the NO predictions in the fuel jet,

see Fig. 12(left), one can observe that the NO reburning rate seems to be over-estimated. Here we recall that in our model the entire volatile matter is involved in the NO-reburning (see Eqs. (43) and (44)) which may be questionable. The second reason is related to the lack of oxygen in the fuel jet obtained in our predictions while in the measurements still around 2% of oxygen can be observed. The oxygen concentration affects strongly the NO-fuel formation path (see Eq. (24)). For the sake of completeness we report that the thermal-NO source (Eq. (36)), the prompt-NO source (Eq. (29)) and the N₂O-NO source (Eq. (39)) are in the range of $0 \div 6.6 \times 10^{-8}$, $0 \div 1.6 \times 10^{-6}$, $0 \div 4.6 \times 10^{-9}$ kmol/m³s, respectively. Integration of the NO sources over an entire furnace volume provides a further insight into the NO-mechanisms. The overall NO production rate through the fuel mechanism is calculated to be 18.5×10^{-6} kg_{NO}/s (see Table 6). The NO reburning rate is 11.5×10^{-6} kg_{NO}/s so that the net NO production rate in the furnace amounts to 7×10^{-6} kg_{NO}/s. The difference between the

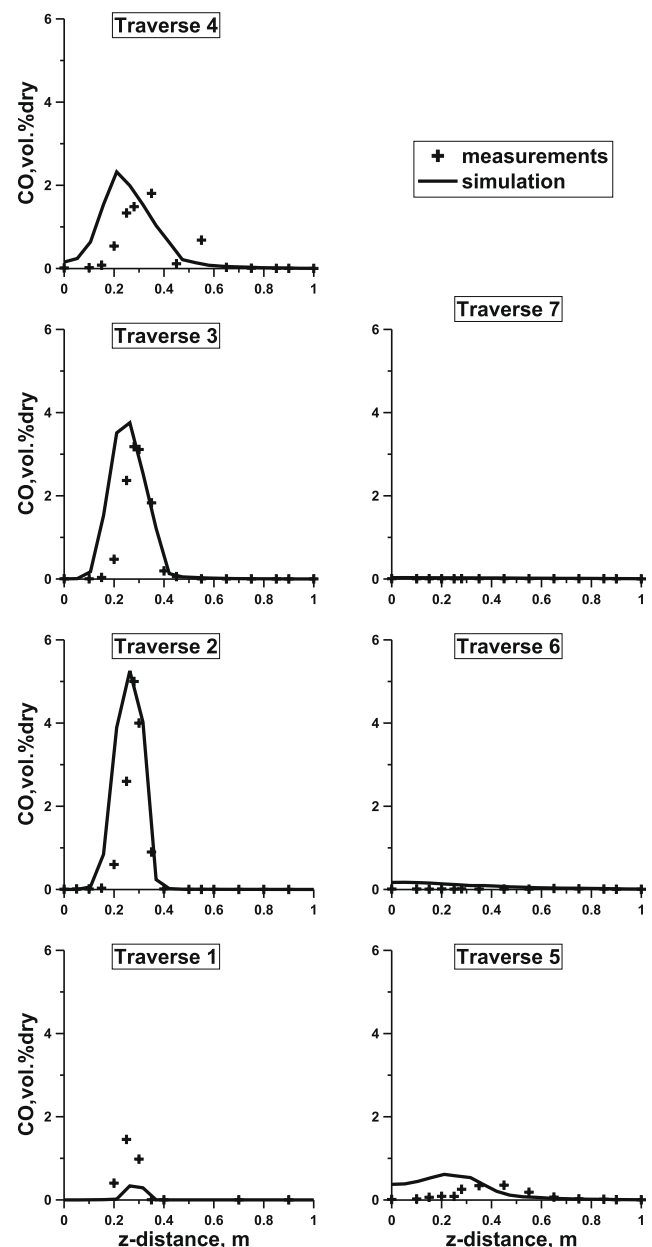


Fig. 11. Carbon monoxide concentration profiles along the measurement traverses. For location of the measurement traverses see Fig. 1.

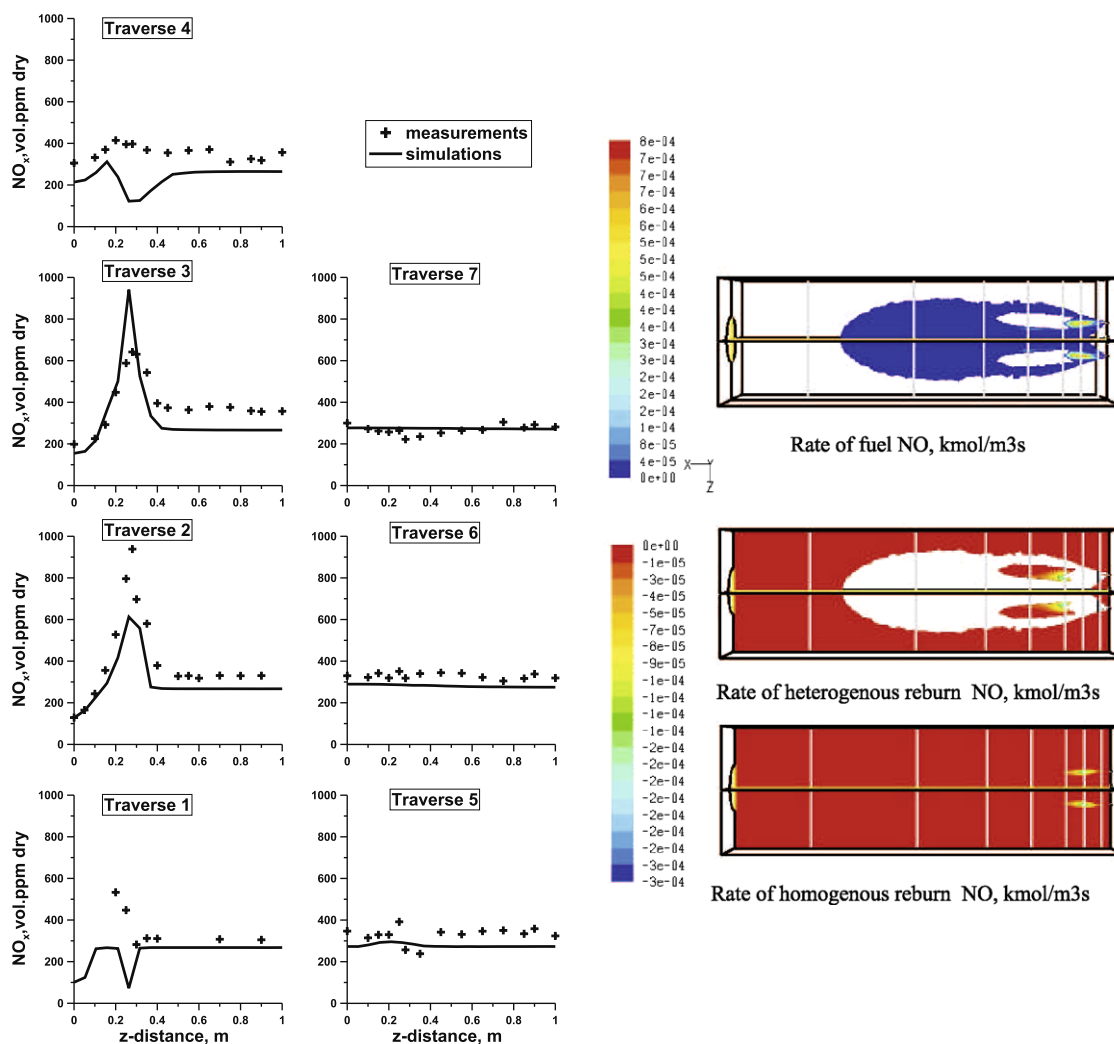


Fig. 12. Nitric oxide (left) along the measurements traverses. Sources in the NO balance equation (right). From the top to the bottom: $S_{NO,fuel}$ – Eq. (27), $S_{NO,heter.reburn}$ – Eq. (47), $S_{NO,hom.reburn}$ – Eq. (45).

Table 6
Mass balance of NO.

$M_{NO,in}$ (kg _{NO} /s)	4.0×10^{-6}
$M_{NO,out}$ (kg _{NO} /s)	-11.0×10^{-6}
$M_{NO,fuel}$ (kg _{NO} /s)	18.5×10^{-6}
$M_{NO,reburn}$ (kg _{NO} /s)	-11.5×10^{-6}

amount of the NO at the furnace exit (11×10^{-6} kg_{NO}/s) and at the furnace inlet (4×10^{-6} kg_{NO}/s) amounts exactly to 7×10^{-6} kg_{NO}/s. Thus, only two terms in the overall NO-balance are significant; the NO generation via the fuel mechanism and the NO reburning mechanism.

4.6. Char burnout

Fig. 13 shows both the measured and predicted char burnout along the centerline of the fuel jet. The char burnout predictions are in good agreement with the measured data up to 80% burnout. For higher degrees of burnout the model over-predicts the char oxidation rates and at the furnace outlet a complete burnout is predicted (see Table 7). This is a consequence of the fact that the parameters of the char combustion model have been derived using the measured data (Fig. 4(right)) that extend up to 85% burnout. As can be seen in Fig. 4(right), an extrapolation of the char model pre-

dictions to residence times of 5–6 s results in complete burnout. In order to predict the last stages of burnout, corrections to the char model are needed to slow down the rate as the char oxidation proceeds (see for example [49,50]).

4.7. Furnace outlet

The temperature, oxygen, carbon oxides and nitric oxide concentrations and char burnout at the outlet of the furnace for calculations and measurements are summarized in Table 7. The furnace exit temperature is very close to the measured value and the difference is about 50 K which corresponds to 2.37% of the furnace thermal input.

5. Conclusions

CFD-based numerical simulations of the IFRF experiment on MILD combustion of coal have been carried out. The burner system consists of a central jet of vitiated air preheated to 1623 K and two jets of pulverized coal. This is indeed a unique burner design as for coal combustion. Prior to performing the numerical simulations substantial efforts have been allocated to an accurate modelling of combustion of Guasare coal which has been used in the IFRF experiment. To this end both the Chemical Percolation Devolatil-

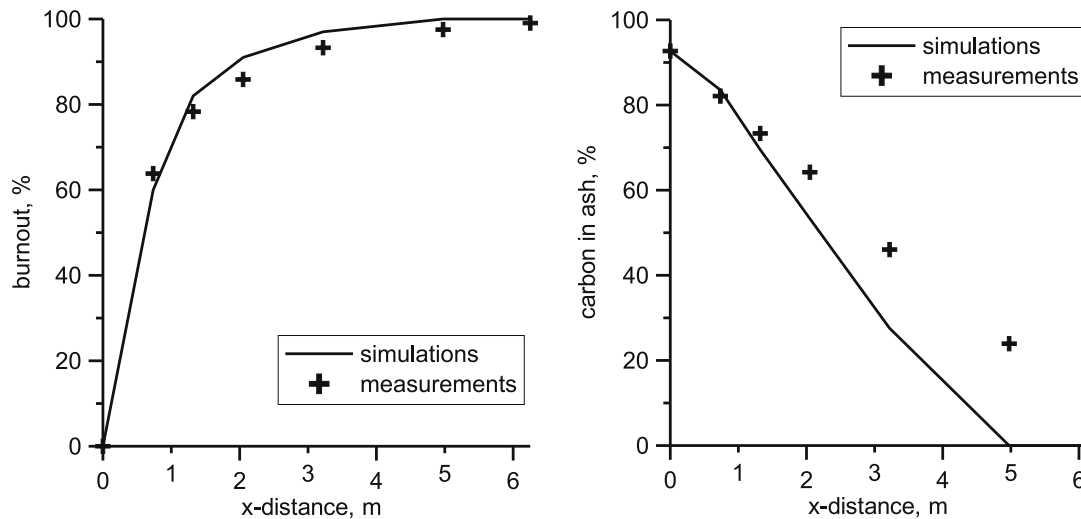


Fig. 13. Char burnout (left) and carbon in ash (right) along the centerline of the fuel jet. The measured values taken from [6].

Table 7

Computed and measured values at the furnace exit.

Parameter	Unit	Experiment [6]	Predictions (this work)
T	K	1503	1555
O_2	vol.% dry	3.1	2.52
CO	vol.ppm dry	<50	10
CO_2	vol.% dry	25.50	23.93
NO_x	vol.ppm dry	320	333
Char burnout	%	99.4	100
Carbon in ash	%	14.95	None

ization (CPD) model and the char combustion intrinsic reactivity model have been adapted to Guasare coal combusted. To ensure accurate predictions of radiative heat transfer, an appropriate value of the local absorption coefficient appearing in the Radiative Transfer Equation has been derived using the measured data. The detailed validation of the predictions against the IFRF in-furnace measurements has led to the following conclusions:

- The flow-field as well as the temperature and oxygen fields have been accurately predicted by the CFD-based model. The predicted temperature and gas composition fields have been uniform demonstrating that slow combustion occurs in the entire furnace volume. Thus, this realization of MILD combustion is inherently different to fast combustion in high gradient fields generated in swirl-stabilized flames.
- The CFD-based predictions have highlighted the NO_x reduction potential of MILD combustion for N -containing fuels through the following mechanism. Before the coal devolatilization proceeds, the coal jet entrains a substantial amount of flue gas so that its oxygen content is typically not more than 3–5%. The volatiles are given off in a highly sub-stoichiometric environment and their N -containing species are preferentially converted to molecular nitrogen rather than to NO . Furthermore, there exist a strong NO -reburning mechanism within the fuel jet and in the air jet downstream of the position where these two jets merge. In other words, less NO is formed from combustion of volatiles and stronger NO -reburning mechanisms exist in the MILD combustion if compared to conventional coal combustion technology.
- Although the carbon monoxide predictions happen to be in very good agreement with the measured values we regard this agreement as coincidental (see text) and more elaborated schemes of

volatile matter combustion are desired. The char burnout figures have been well predicted until 80% of burnout. However, corrections to the char model are needed to slow down the rate as the char oxidation proceeds further.

Acknowledgments

The work has been carried out within the European Commission Marie Curie INSPIRE Network (MRTN-CT-2005-019296) and the Project of Polish Ministry of Education and Science (2908/T02/2007/32). The authors acknowledge with thanks the financing.

References

- [1] Key World Energy Statistics, The International Energy Agency, IEA, 2007. Available from: <<http://www.iea.com>>.
- [2] H. Tsuji, A.K. Gupta, T. Hasegawa, M. Katsuki, K. Kishimoto, M. Morita, High Temperature Air Combustion: From Energy Conservation to Pollution Reduction, CRC Press, Boca Raton, FL, 2003.
- [3] M. Mancini, Analysis of mild combustion of natural gas with preheated air, Ph.D. Thesis, Clausthal University of Technology, Faculty of Energy and Economics, 2007.
- [4] R. Weber, M. Mancini, Recent developments in flameless combustion technology, in: Proceedings of the 8th European Conference on Industrial Furnaces and Boilers, Vilamoura, Portugal, 2008.
- [5] A. Cavaliere, M.D. de Joannon, Mild combustion, Prog. Energy Combust. Sci. 30 (2004) 329–366.
- [6] S. Orsino, M. Tamura, P. Stabat, S. Costantini, O. Prado, R. Weber, Excess enthalpy combustion of coal, Results of HTAC 99 trials, Technical Report IFRF Doc. No. F46/y/3, IFRF Research Report, Ijmuiden, 2000.
- [7] R. Weber, J. Smart, W. VdKamp, On the MILD combustion of gaseous, liquid, and solid fuels in high temperature preheated air, Proc. Combust. Inst. 30 (2005) 2623–2629.
- [8] R. Weber, Combustion of natural gas, oil and coal with air preheated to temperatures in excess of 1000 °C, in: Proceedings of the 13th IFRF Members Conference, Noordwijkerhout, The Netherlands, 2001.
- [9] FLOX-coal development of a pilot scale flameless oxidation burner for ultra low NO_x combustion of pulverized coal, European Commission (Research Fund for Coal and Steel), RFCR-CR-2005-00010.
- [10] D. Ristic, A. Schuster, G. Scheffknecht, H. Stadler, M. Foerster, R. Kneer, J.G. Wünnig, Experimental study on flameless oxidation of pulverised coal in bench and pilot scale, in: Proceedings of the 23th German Flameday, Berlin, Germany, 2007.
- [11] D. Ristic, M. Schneider, A. Schuster, G. Scheffknecht, J.G. Wünnig, Investigation of NO_x formation for flameless coal combustion, in: Proceedings of the 7th HiTAC Symposium, Phuket, Thailand, 2008.
- [12] S. Löhr, M. Kretschmann, S. Wirtz, V. Scherer, Pyrolyse und Flüchtigenabbrand von Kraftwerkskohlen bei niedrigen Sauerstoffkonzentrationen, in: Proceedings of the 23th German Flameday, Berlin, Germany, 2007 (in German).
- [13] Untersuchungen zur Schadstoffbildung bei der FLOX-Verbrennung von Kohlestaub, DFG (German Research Foundation), Gz.: SCHE 322/4-2 (in German).

- [14] T. Suda, M. Takafuji, T. Hirata, M. Yoshino, J. Sato, A study of combustion behavior of pulverized coal in high-temperature air, *Proc. Combust. Inst.* 29 (2002) 503–509.
- [15] R. He, T. Suda, M. Takafuji, T. Hirata, J. Sato, Analysis of low NO emission in high temperature air combustion for pulverized coal, *Fuel* 83 (2004) 1133–1141.
- [16] P. Heil, U. Renz, R. Kneer, Experimentelle Untersuchung eines FLOX-Brenners bei Druckkohlenstaubfeuerungsbetrieb, in: 4. Druckflamm Seminar, Dortmund, Germany, 2004 (in German).
- [17] J. Erfurth, D. Toporov, S. Tschunko, C. von Petry, R. Kneer, Modellierung der flammlosen Verbrennung in einer Druckkohlenstaubfeuerung, in: 22th German Flameday, Braunschweig, Germany, 2005 (in German).
- [18] J.P. Kim, U. Schnell, G. Scheffknecht, A.C. Benim, Numerical modeling of MILD combustion for coal, *Prog. Comput. Fluid Dynamics* 7 (2007) 337–346.
- [19] J.P. Kim, Numerical modeling of MILD combustion, Ph.D. Thesis, University of Stuttgart, 2008.
- [20] D. Förtsch, A kinetic model of pulverised coal combustion for computational fluid dynamics, Ph.D. Thesis, University of Stuttgart, 2003.
- [21] D. Förtsch, F. Kluger, U. Schnell, H. Spliethoff, K.R.G. Hein, A kinetic model for the prediction of NO emissions from staged combustion of pulverized coal, *Proc. Combust. Inst.* 27 (1998) 3037–3044.
- [22] P.R. Solomon, T.H. Fletcher, R.J. Pugmire, Progress in coal pyrolysis, *Fuel* 72 (1993) 587–597.
- [23] M. Tamura, Data on characterization of Guasare coal, 2000. (unpublished).
- [24] S. Badzioch, P.G.W. Hawksley, Kinetics of thermal decomposition of pulverized coal particles, *Ind. Eng. Chem. Process Des. Develop.* 9 (1970) 521–530.
- [25] H. Kobayashi, J.B. Howard, A.F. Sarofim, Coal devolatilization at high temperatures, *Proc. Combust. Inst.* 16 (1976) 411–425.
- [26] D.M. Grant, R.J. Pugmire, T.H. Fletcher, A.R. Kerstein, Chemical model of coal devolatilization using percolation lattice statistics 3 (1989) 175–186.
- [27] T.H. Fletcher, A.R. Kerstein, R.J. Pugmire, D.M. Grant, Chemical percolation model for devolatilization: 2. Temperature and heating rate effects on product yields, *Energy Fuels* 4 (1990) 54–60.
- [28] T.H. Fletcher, A.R. Kerstein, Chemical percolation model for devolatilization: 3. Direct Use of ^{13}C NMR data to predict effects of coal type, *Energy Fuels* 6 (1992) 414–431.
- [29] I.W. Smith, The combustion rates of coal chars: a review, *Proc. Combust. Inst.* 19 (1982) 1045–1065.
- [30] B.E. Launder, D.B. Spalding, The numerical computation of turbulent flows, *Comput. Meth. Appl. Mech. Eng.* 3 (1974) 269–289.
- [31] B.F. Magnussen, B.H. Hjertager, On mathematical modeling of turbulent combustion with special emphasis on soot formation and combustion, *Proc. Combust. Inst.* 16 (1976) 719–729.
- [32] F. Boysan, W.H. Ayers, J. Swithenbank, Fundamental mathematical modelling approach to cyclone design, *Trans. I. Chem. E* 60 (1982) 222–230.
- [33] R. Weber, F. Boysan, W.H. Ayers, J. Swithenbank, Simulation of dispersion of heavy particles in confined turbulent flows, *AIChE J.* 30 (1984) 490–492.
- [34] W.A. Fiveland, A.S. Jamaluddin, Three-dimensional radiative heat transfer solutions by the discrete-ordinates method, *J. Thermophysics* 2 (1988) 309–316.
- [35] J.S. Truelove, Three-dimensional radiation in absorbing-emitting-scattering using the discrete-ordinates approximation, *JQSRT* 39 (1988) 27–31.
- [36] G. Hand, M. Missaghi, M. Pourkashanian, A. Williams, Experimental studies and computer modeling of nitric oxides in a cylindrical natural gas fired furnace, in: Proceedings of the 9th IFRF Members Conference, Noordwijkerhout, The Netherlands, 1989.
- [37] A.A.F. Peters, R. Weber, Modeling of a 2.25 MW_{th} swirling natural gas flame. Part I: Eddy break-up concept for turbulent combustion; Probability density function approach for nitric oxide formation, *Combust. Sci. Technol.* 110–111 (1995) 67–101.
- [38] G.G. De Soete, Overall reaction rates of NO and N₂ formation from fuel nitrogen, *Proc. Combust. Inst.* 15 (1975) 1093–1102.
- [39] M. Missaghi, M. Pourkashanian, A. Williams, L. Yap, The prediction of NO emission from an industrial burner, in: Proceeding of American Flame Days Conference, San Francisco, USA, 1990.
- [40] P. Melte, D. Pratt, Measurements of atomic oxygen and nitrogen oxides in jet stirred combustion, *Proc. Combust. Inst.* 15 (1974) 1061–1070.
- [41] W. Chen, L.D. Smoot, T.H. Fletcher, R.D. Boardman, Global rate expression for nitric oxide reburning. Part II, *Energy Fuels* 10 (1999) 1046–1056.
- [42] W. Chen, L.D. Smoot, S.C. Hill, T.H. Fletcher, A computational method for determining global fuel–NO rate expressions. Part I, *Energy Fuels* 10 (1999) 1036–1046.
- [43] J.M. Levy, L.K. Chen, A.F. Sarofim, J.M. Beer, NO/Char reactions at pulverized coal flame conditions, *Proc. Combust. Inst.* 18 (1981) 340–343.
- [44] N. Lallemant, A. Sayre, R. Weber, Evaluation of emissivity correlations for H₂O–CO₂–N₂/air mixtures and coupling with solution methods of the radiative transfer equation, *Prog. Energy Combust. Sci.* 22 (1990) 543–574.
- [45] A. Sayre, N. Lallemant, J. Dugué, R. Weber, Effect of radiation on nitrogen emissions from non-sooty swirling flames of natural gas, *Proc. Combust. Inst.* 25 (1994) 235–242.
- [46] R. Weber, A. Verlaan, S. Orsino, N. Lallemant, Combustion of natural gas with high temperature air and large quantities of flue gas, *Proc. Combust. Inst.* 28 (2000) 1315–1321.
- [47] R. Weber, A. Verlaan, S. Orsino, N. Lallemant, On emerging furnace design methodology that provides substantial energy savings and drastic reductions in CO₂, CO and NO_x emissions, *J. Inst. Energy* 72 (1999) 77–83.
- [48] M. Mancini, P. Schwöppe, R. Weber, S. Orsino, On mathematical modeling of flameless combustion, *Combust. Flame* 150 (2007) 54–59.
- [49] A.A.F. Peters, R. Weber, Mathematical modeling of a 2.4 MW_{th} swirling pulverized coal flame, *Combust. Sci. Technol.* 122 (1997) 131–182.
- [50] J. Haas, Experimentelle Untersuchungen der Reaktivität von Kohlenkoks zur Modellierung seines Verbrennungsverhaltens in Staubfeuerungen, Ph.D. Thesis, Faculty of Energy and Management, Clausthal University of Technology, 1999 (in German).